Electronic structure and thermodynamic properties of $CeRh_2Sn_4$ and $LaRh_2Sn_4$

# Electronic structure and thermodynamic properties of CeRh₂Sn₄ and LaRh₂Sn₄

## M Gamża[1,2], W Schnelle[2], R Gumeniuk[2], Yu Prots[2], A Ślebarski[1], H Rosner[2] and Yu Grin[2]

[1] Institute of Physics, University of Silesia, PL-40-007 Katowice, Poland
[2] Max-Planck Institute for Chemical Physics of Solids, D-01187 Dresden, Germany

E-mail: monikag3@o2.pl, andrzej.slebarski@us.edu.pl and rosner@cpfs.mpg.de

**Abstract**

The electronic structure and thermodynamic properties of CeRh₂Sn₄ and LaRh₂Sn₄ are reported. The crystal structure of CeRh₂Sn₄ has been determined from single-crystal diffraction experiments. The Ce core-level x-ray photoemission spectra and Ce L$_{III}$ x-ray absorption data unanimously indicate a stable trivalent state of the Ce ions in CeRh₂Sn₄, consistent with static magnetic susceptibility. Thermodynamic measurements for CeRh₂Sn₄ show a noncollinear antiferromagnetic ordering with a ferromagnetic component at $T_N \approx 3.2$ K. There is evidence for spin fluctuations in both CeRh₂Sn₄ and LaRh₂Sn₄. A Fermi surface analysis reveals sections, which could generate 'nesting' instabilities and be responsible for the spin fluctuation effects. Both CeRh₂Sn₄ and LaRh₂Sn₄ exhibit slight homogeneity ranges and can be described by RE$_{1+x}$Rh₂Sn$_{4-x}$, where $0 \leqslant x \lesssim 0.2$ for Ce and $0 \leqslant x \lesssim 0.1$ in the case of La. Implantation of additional Ce atoms into the CeRh₂Sn₄ structure leads to a distinct lowering of $T_N$ and the weakening of the ferromagnetic component of the magnetic ground state, whereas for the La-based systems the alloying reduces the strong diamagnetism.

(Some figures in this article are in colour only in the electronic version)

## 1. Introduction

A large number of Ce-based intermetallics are known to be materials, in which the electrons of the 4f shell strongly interact with conduction band electrons [1]. This interaction gives rise to two competing processes, which determine the ground state properties of Kondo lattice systems: the long-range Ruderman–Kittel–Kasuya–Yosida (RKKY) interaction between the local 4f magnetic moments mediated by the conduction electrons and the on-site Kondo screening of the localized Ce 4f moments by the band states. The strength of these two mechanisms is measured by $|J_{sf}N(E_F)|$, where $J_{sf}$ is the antiferromagnetic exchange coupling of the local 4f moments and the conduction electron spins and $N(E_F)$ is the density of states (DOS) at the Fermi level $E_F$. In the weak coupling limit, the RKKY interaction dominates and consequently a long-range magnetic order occurs. At the other extreme, the Kondo effect suppresses the Ce 4f moments and leads to the formation of nonmagnetic ground states. In this regime the Ce ions are often in an intermediate valence state and both charge and spin fluctuations play an important role

in the physical properties of such materials. The case of medium $|J_{sf}N(E_F)|$ values is very interesting. Here, the strong interplay of Kondo and RKKY interactions can result in diverse intriguing strongly correlated electron phenomena, including magnetism with reduced moments, non-Fermi liquid behaviour or unconventional superconductivity in the vicinity of the quantum phase transition from the heavy-fermion magnetically ordered to the nonmagnetic Fermi liquid state.

During the last few years, several intermetallics from the ternary Ce–Rh–Sn system, in particular CeRhSn₂, Ce₅Rh₄Sn₁₀ and Ce₂Rh₃Sn₅, were reported to be magnetically ordered Kondo lattice systems [2–4]. In all these phases the magnetic moments of Ce ions are rather localized, yielding a paramagnetic Curie–Weiss-type behaviour at elevated temperatures. At low temperatures the Kondo effect results in the formation of heavy quasi-particle bands in the vicinity of the Fermi level, which manifest themselves, for example, in a distinct enhancement of the electronic specific heat. The Sommerfeld coefficient attains values from $\sim$100 mJ Ce-mol$^{-1}$ K$^{-2}$ in Ce₅Rh₄Sn₁₀ [2] to $\sim$300 mJ Ce-mol$^{-1}$ K$^{-2}$ in CeRhSn₂ [3]. Among this group of

intermetallics, CeRhSn has attracted special interest due to its non-Fermi liquid behaviour at low temperatures indicated by electrical resistivity, specific heat and magnetic susceptibility measurements [5, 6]. This system is supposed to be located on the border between a nonmagnetic and a magnetically ordered ground state, presumably in the vicinity of the antiferromagnetic instability, as indicated by nuclear magnetic resonance results [7]. Simultaneously, the anomalous volume deviation from the usual lanthanide contraction, the thermodynamic data as well as photoemission spectra [5, 8, 9] indicate an intermediate valence state of the Ce ions in this compound. In addition, for CeRhSn spin fluctuations due to the Rh 4d electrons were suggested [10]. Spin fluctuations related to the Rh 4d states have also been detected for the compound CeRhSn$_2$ [11].

In view of these intriguing physical phenomena, it is of interest to investigate in detail another member of this group, the compound CeRh$_2$Sn$_4$. In this contribution we report the results of magnetization, static and dynamic magnetic susceptibility, electrical resistivity and specific heat measurements on CeRh$_2$Sn$_4$ and the isostructural reference system LaRh$_2$Sn$_4$. In addition, we present the extended study [12] of the electronic band structure based on x-ray photoemission spectroscopy (XPS) and x-ray absorption spectroscopy (XAS) at the Ce L$_{III}$ threshold as well as first-principles calculations. The results for CeRh$_2$Sn$_4$ are analysed together with the corresponding data for the reference compound LaRh$_2$Sn$_4$.

Méot-Meyer *et al* [13] suggested that the systems CeRh$_2$Sn$_4$ and LaRh$_2$Sn$_4$ have some homogeneity ranges related to the partial occupancy of one of the Sn sites by rare-earth (RE) atoms. Therefore a series of polycrystalline samples with the nominal composition RE$_{1+x}$Rh$_2$Sn$_{4-x}$ ($0 \leqslant x \lesssim 0.4$; RE = Ce or La) were prepared. Some of these samples were a subject of consecutive studies. Single crystals of CeRh$_2$Sn$_4$ have been investigated in order to determine the crystal structure of the stoichiometric compound.

## 2. Methods

### 2.1. Experimental details

A series of samples with the nominal compositions RE$_{1+x}$Rh$_2$Sn$_{4-x}$ ($0 \leqslant x \leqslant 0.4$; RE = Ce or La) were prepared from ingots of cerium (Ames, 99.9 wt%) and lanthanum (Ames, 99.9 wt%), rhodium granules (ChemPur, 99.9 wt%) and tin foil (ChemPur, 99.99 wt%). All samples with a total mass of about 2 g were arc-melted without remarkable losses. Subsequently obtained ingots were sealed in Ta tubes and heat-treated in evacuated quartz ampoules at 950 °C for 4 d. Finally they were quenched in cold water without breaking the ampoules.

Phase analysis of the polycrystalline samples was carried out from x-ray powder diffraction patterns collected on a HUBER imaging plate Guinier camera G670 (Cu K$\alpha_1$ radiation, $2\theta$ interval of 3°–100°, exposure time 6 min × 15 min). The orthorhombic lattice parameters were refined by least-squares fittings of Guinier powder data with LaB$_6$ as

**Table 1.** Crystallographic data for CeRh$_2$Sn$_4$.

| | |
|---|---|
| Empirical formula | CeRh$_2$Sn$_4$ |
| Structure type | NdRh$_2$Sn$_4$ |
| Space group | *Pnma* (No. 62) |
| Lattice parameters$^a$ | $a = 18.4371(9)$ Å |
| | $b = 4.5035(3)$ Å |
| | $c = 7.1308(5)$ Å |
| Formula units/cell, $Z$ | 4 |
| Diffraction system | Rigaku AFC7, |
| | Mercury CCD detector |
| Radiation, $\lambda$ (Å) | Mo K$\alpha$, 0.710 73 |
| $2\theta_{max}$ and $\sin\theta/\lambda_{max}$ | 61.95°, 0.724 |
| Range in $h, k, l$ | $\pm24, \pm5, \pm9$ |
| N ($hkl$) measured | 4259 |
| N ($hkl$) unique | 938 |
| $R(eqv)/R(\sigma)$ | 0.032/0.025 |
| N ($hkl$) observed | 817 |
| Observation criteria | $F(hkl) > 4.00\sigma(F)$ |
| Extinction parameter | 0.000 27(8) |
| Refined parameters | 57 |
| $R(F)$ | 0.029 |

$^a$ Powder data.

internal standard ($a = 4.15692$ Å). The investigated samples were found to consist of a single phase, with the exception of LaRh$_2$Sn$_4$, where the analysis revealed a small amount of minority phase La$_3$Rh$_4$Sn$_{13}$ (less than 2 vol% in the bulk sample). The obtained samples were fine crystalline and did not contain a suitable specimen for single-crystal diffraction.

To synthesize single crystals of CeRh$_2$Sn$_4$ suitable for x-ray diffraction investigation, a stoichiometric mixture of elemental components was melted in glassy carbon crucibles at 1300 °C using a high-frequency furnace, and then cooled down to 750 °C within 15 min. The sample was thermally treated as described above. Several irregularly shaped crystals of CeRh$_2$Sn$_4$ were mechanically extracted from the annealed ingot. The x-ray diffraction studies were carried out on a Rigaku AFC7 diffractometer equipped with a mercury CCD detector applying Mo K$\alpha$ radiation ($\lambda = 0.71073$ Å). Details concerning the data collection and handling are summarized in table 1. All crystallographic calculations were performed by using the WinCSD program package [14].

We succeeded also in the growth of CeRh$_2$Sn$_4$ crystals of larger size ($1 \times 1 \times 3$ mm$^3$), which were the subject of thermodynamic studies. The crystals were obtained by the following procedure: powders of Ce (Goodfellow, 99.9 wt%), Rh (Heraeus, 99.9 wt%) and Sn (ChemPur, 99.95 wt%) with a total mass of 5 g were carefully mixed and pressed into a pellet, which was placed in a glassy carbon crucible, sealed in a Ta tube and heated inside an evacuated quartz ampoule up to 1250 °C and then slowly (3 °C h$^{-1}$) cooled down to 600 °C. One of the extracted crystalline specimens is presented in figure 1.

To prevent the oxidation of elemental cerium and lanthanum all manipulations connected with sample preparation were performed in an argon-filled glove box (MBRAUN, $p(O_2/H_2O) \leqslant 1$ ppm).

Differential thermal analysis (DTA) was performed using an STA 449C NETZSCH device (Al$_2$O$_3$ crucibles, sample mass ~100 mg) under argon atmosphere in the temperature

**Table 2.** Lattice parameters, phase composition and results of EDXS and WDXS analyses for some of the $RE_{1+x}Rh_2Sn_{4-x}$ samples (RE = Ce or La).

| Nominal composition | Phase analysis | Lattice parameters | Composition from EDXS and WDXS* |
|---|---|---|---|
| $CeRh_2Sn_4$ | $CeRh_2Sn_4$ | $a = 18.4371(9)$ Å<br>$b = 4.5035(3)$ Å<br>$c = 7.1308(5)$ Å<br>$V = 592.1(1)$ Å$^3$ | $Ce_{1.0(1)}Rh_{2.0(1)}Sn_{4.0(1)}$ |
| $Ce_{1.2}Rh_2Sn_{3.8}$ | $Ce_{1.2}Rh_2Sn_{3.8}$ | $a = 18.5174(3)$ Å<br>$b = 4.4984(1)$ Å<br>$c = 7.1836(1)$ Å<br>$V = 598.38(3)$ Å$^3$ | $Ce_{1.3(1)}Rh_{2.0(1)}Sn_{3.7(1)}$<br>$Ce_{1.18(4)}Rh_{2.01(1)}Sn_{3.81(3)}$* |
| $LaRh_2Sn_4$ | $LaRh_2Sn_4$ +<br>$La_3Rh_4Sn_{13}$ ($\leqslant$2 vol%) | $a = 18.4924(9)$ Å<br><br>$b = 4.5287(2)$ Å<br>$c = 7.1350(3)$ Å<br>$V = 597.5(1)$ Å$^3$ | $La_{1.0(1)}Rh_{2.0(1)}Sn_{4.0(1)}$ |
| $La_{1.1}Rh_2Sn_{3.9}$ | $La_{1.1}Rh_2Sn_{3.9}$ | $a = 18.5457(2)$ Å<br>$b = 4.5262(1)$ Å<br>$c = 7.1687(1)$ Å<br>$V = 601.75(2)$ Å$^3$ | $La_{1.1(1)}Rh_{2.0(1)}Sn_{3.9(1)}$ |
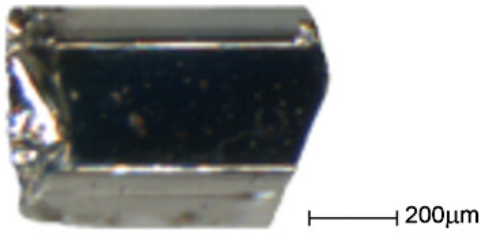


**Figure 1.** Image of a crystal of $CeRh_2Sn_4$.

range of 30–1300 °C with a heating rate 10 °C min$^{-1}$. The calibration was done using five melting standards (thermocouple type S).

For metallographic examination, pieces of about 3 mm diameter were cut from the annealed samples and embedded in epoxy resin. Grinding was performed on abrasive papers (500- and 1000-grit silicon carbide). Polishing was done using slurries of 9 and 3 $\mu$m diamond powder in alcohol-based lubricants. The microstructures were examined optically (Zeiss Axioplan 2) and with a scanning electron microscope (Philips XL 30). The compositions of the observed phases were analysed by energy dispersive x-ray spectroscopy (EDXS, Philips XL 30) and wavelength dispersive x-ray spectroscopy (WDXS, Cameca SX 100) by using $CeAl_2$, Rh and Sn as standards. The intensities of the lines Ce L$\alpha$, Rh L$\alpha$ and Sn L$\alpha$ were determined at an excitation current LPC3 of 15 nA at 25 keV. Results from EDXS and WDXS analysis are in good agreement with phase analysis deduced from powder x-ray diffraction data and nominal compositions of the samples (see table 2).

The Ce L$_{III}$ XAS spectra were recorded in a transmission arrangement at the EXAFS beamline A1 of HASYLAB at DESY at the temperatures of 80 and 293 K. The wavelength selection was realized using the four-crystal mode which

yielded an experimental resolution of ∼2 eV (FWHM) at the Ce L$_{III}$ threshold of 5723 eV. Experimental data were measured using $CeO_2$ as an external reference compound.

The XPS spectra were obtained with monochromatized Al K$\alpha$ radiation at room temperature using a PHI 5700 ESCA spectrometer. Polycrystalline samples were broken under a high vacuum of $3 \times 10^{-8}$ Pa immediately before taking spectra. Calibration of the spectra was performed according to [15]. Binding energies were referenced to the Fermi level ($E_F = 0$).

The magnetization studies were carried out in a SQUID magnetometer (MPMS XL-7, Quantum Design) in magnetic fields 20 Oe $\leqslant H \leqslant$ 70 kOe between 1.8 and 400 K. Heat capacity was determined by a relaxation-type method using a commercial system (PPMS, Quantum Design). Electrical resistivity measurements were performed on polycrystalline pieces with a standard dc four-probe set-up at temperatures between 4 and 320 K. The dynamic magnetic susceptibility was measured in the temperature range of 1.8–300 K using a commercial ac susceptometer (Lake-Shore). The amplitude of the excitation field was 10 Oe at a fixed frequency of 10 kHz.

*2.2. Computational*

The electronic structure of both stoichiometric compounds $CeRh_2Sn_4$ and $LaRh_2Sn_4$ is studied using the full potential local orbital (FPLO) minimum basis code (version 5.00-19) [16] within the local spin density approximation (LSDA). In the scalar-relativistic calculations the exchange–correlation (XC) potential of Perdew and Wang was employed [17]. As a basis set, Ce (4f5s5p/5d6s6p), La (5s5p/5d6s6p:4f), Rh (4s4p/4d5s5p) and Sn (4s4p4d/5s5p:5d) states were employed as semi-core/valence:polarization states. The lower-lying states were treated fully relativistically as core states. The inclusion of semi-core states was extorted by their non-negligible overlap with orbitals on neighbouring atoms which

results in a non-negligible bandwidth. The La 4f and Sn 5d states were taken into account as polarization states to improve the completeness of the basis set. The spatial extension of the basis orbitals, controlled by the confining potential exponent equal to 5, was optimized to minimize the total energy [18]. The strong Coulomb correlation within the Ce 4f shell was treated in a mean-field way using the LSDA + $U$ method [19] (applying the around-mean-field double-counting scheme). The Coulomb repulsion $U$ and exchange constant $J$ for the Ce 4f states were assumed to be 3.5–8 eV and 0–0.7 eV, respectively. The Brillouin zone was sampled by a $k$-mesh containing 60 irreducible points. In the antiferromagnetic calculations for CeRh$_2$Sn$_4$ a similar density of $k$-mesh was assumed.

Based on the band structure results we calculated the theoretical XPS valence band spectra. The partial $l$-resolved DOSs were multiplied by the corresponding atomic-like photoemission cross sections [20] and convoluted by the Lorentzians with a full width at half-maximum of 0.4 eV to account for the instrumental resolution, thermal broadening and the effect of the lifetime of the hole states. The results were convoluted by the Fermi–Dirac function for 300 K.

To optimize atomic positions in crystal lattices based on atomic forces we performed also band structure calculations by the full potential linearized augmented plane-wave (FP-LAPW) method [21] using the Wien2k computer code [22] for both CeRh$_2$Sn$_4$ and LaRh$_2$Sn$_4$. The resulting total DOSs and band structures were basically identical for the two band structure codes.

To evaluate a functional termed the electron localizability indicator (ELI) we used the TB-LMTO-ASA program package [23]. In the calculations atomic coordinates from the structural optimization (see below) and the experimentally obtained lattice parameters were assumed. The Barth–Hedin exchange potential [24] was used within the LDA calculations. The radial scalar-relativistic Dirac equation was solved to get the partial waves. Because the calculation within the atomic sphere approximation (ASA) includes corrections for the neglect of interstitial regions and partial waves of higher order [25] an addition of empty spheres was not necessary. The following radii of the atomic spheres were chosen: $r(La) = 2.039$ Å, $r(Rh1) = 1.568$ Å, $r(Rh2) = 1.569$ Å, $r(Sn1) = 1.676$ Å, $r(Sn2) = 1.743$ Å, $r(Sn3) = 1.681$ Å and $r(Sn4) = 1.675$ Å. A basis set containing La(6s5d4f), Sn(5s5p) and Rh(5s5p4d) orbitals was employed for a self-consistent calculation with La(6p), Sn(5d4f) and Rh(4f) functions being downfolded. Comparing DOSs obtained within the ASA approximation with those derived from the full potential band structure codes we ensured the sufficient accuracy of the calculations performed using the TB-LMTO-ASA code. The electron localizability indicator (ELI, $\Upsilon$) [26] was evaluated in the ELI-D representation according to [27, 28] with an ELI-D module included in the TB-LMTO-ASA program package. The procedure for calculation of the partial ELI-D contributions from different energy ranges in the electronic DOS was implemented in the TB-LMTO-ASA code. ELI-D and electron density were analysed using the program Basin [29] with consecutive integration of the electron density
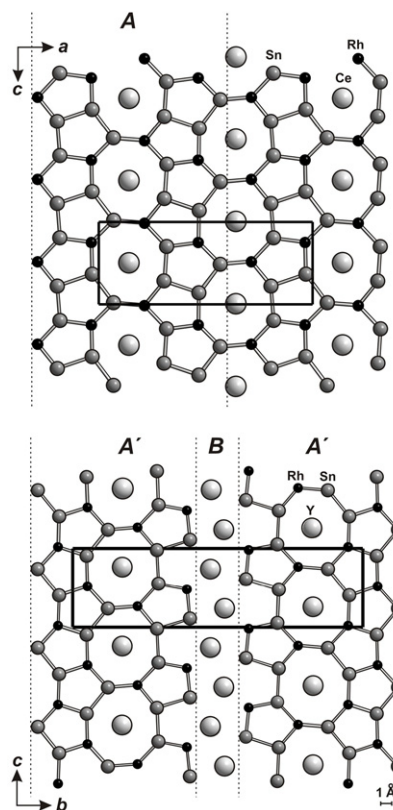


**Figure 2.** Fragments of the crystal structures of CeRh$_2$Sn$_4$ (upper panel) and Y$_2$Rh$_3$Sn$_5$ (lower panel) in the projection along [0 1 0] and [1 0 0] at $y = 0$ and $x = 1/4$, respectively. Similar topology of planar nets has been emphasized.

in basins, which are bound by zero-flux surfaces in the ELI-D or electron density gradient field. Such a treatment of ELI-D is similar to the procedure proposed by Bader for the electron density [30].

## 3. Results and discussion

### 3.1. Crystal structure of CeRh$_2$Sn$_4$

The crystal structure of CeRh$_2$Sn$_4$ was determined from single-crystal diffraction data. The studies performed confirm that CeRh$_2$Sn$_4$ adopts the NdRh$_2$Sn$_4$ structure type as was assumed earlier [13]. For the first time, however, the refinement of the representative of this structure type from x-ray powder data resulted in a fully ordered structure with complete occupancy of all crystallographic sites. The obtained lattice parameters, atomic coordinates and displacement parameters are listed in tables 1 and 3. The stoichiometric composition of CeRh$_2$Sn$_4$ was also confirmed by EDXS study (table 2).

In the crystal structure of CeRh$_2$Sn$_4$ rhodium and tin species form a three-dimensional (3D) polyanion in which Ce atoms are embedded. For better visualization we cut this polyanion into sets of planar nets stretched perpendicular to [0 1 0] in heights of $y = 1/4$ and $3/4$ and present in figure 2 only the atoms situated at $y = 1/4$.

Selected interatomic distances in CeRh$_2$Sn$_4$ are listed in table 4. The Rh–Sn distances within the 3D polyanion vary between 2.6880(7) and 2.8648(8) Å. The shortest Sn–Sn contact occurs at 2.984(1) Å between Sn2 and Sn3. Further

**Table 3.** Atomic positional and displacement parameters for $CeRh_2Sn_4$. (Note: $B_{12} = B_{23} = 0$.) All atoms are located at 4c Wyckoff positions ($x$, 1/4, $z$).

| Atom | $x$ | $z$ | $B_{11}$ | $B_{22}$ | $B_{33}$ | $B_{13}$ | $B_{eq}$ |
|------|------|------|------|------|------|------|------|
| Ce | 0.358 51(4) | 0.0005(1) | 0.73(3) | 0.59(3) | 0.79(3) | 0.04(2) | 0.70(2) |
| Rh1 | 0.034 95(5) | 0.7501(1) | 0.84(3) | 0.74(4) | 0.79(4) | −0.01(3) | 0.79(2) |
| Rh2 | 0.286 15(5) | 0.5158(1) | 0.89(3) | 0.60(4) | 0.71(4) | −0.00(3) | 0.73(2) |
| Sn1 | 0.031 47(5) | 0.3635(1) | 0.73(3) | 0.69(3) | 0.78(3) | −0.02(2) | 0.73(2) |
| Sn2 | 0.182 28(5) | 0.8024(1) | 0.86(3) | 0.62(3) | 0.67(3) | −0.02(2) | 0.72(2) |
| Sn3 | 0.194 54(5) | 0.2196(1) | 0.84(3) | 0.68(3) | 0.60(3) | 0.03(2) | 0.71(2) |
| Sn4 | 0.431 71(4) | 0.4830(1) | 0.59(3) | 0.79(3) | 0.70(3) | −0.06(2) | 0.69(2) |

**Table 4.** Selected interatomic distances in $CeRh_2Sn_4$.

| Atoms | $d$ (Å) | Atoms | $d$ (Å) | Atoms | $d$ (Å) |
|-------|---------|-------|---------|-------|---------|
| Ce–2Sn3 | 3.1681(8) | Rh2–1Sn3 | 2.7039(8) | Sn2–2Sn4 | 3.3384(9) |
| 2Sn1 | 3.1844(8) | 2Sn3 | 2.704(1) | 1Ce | 3.543(1) |
| 2Sn2 | 3.2049(8) | 2Sn2 | 2.7792(8) | Sn3–2Rh2 | 2.7039(8) |
| 1Sn1 | 3.333(1) | 1Sn2 | 2.801(1) | 1Rh2 | 2.704(1) |
| 1Sn3 | 3.403(1) | 2Ce | 3.4921(9) | 1Sn2 | 2.984(1) |
| 2Rh1 | 3.4783(9) | 1Ce | 3.705(1) | 2Ce | 3.1681(8) |
| 2Rh2 | 3.4921(9) | 1Ce | 3.909(1) | 1Sn1 | 3.177(1) |
| 1Sn2 | 3.543(1) | Sn1–2Rh1 | 2.6880(7) | 2Sn2 | 3.2524(9) |
| 1Sn4 | 3.696(1) | 1Rh1 | 2.758(1) | 1Ce | 3.403(1) |
| 1Rh2 | 3.705(1) | 1Sn4 | 3.080(1) | 2Sn4 | 3.6516(9) |
| 1Rh1 | 3.712(1) | 1Sn3 | 3.177(1) | Sn4–1Rh1 | 2.692(1) |
| 1Rh2 | 3.909(1) | 2Ce | 3.1844(8) | 1Rh2 | 2.694(1) |
| 1Sn4 | 3.929(1) | 2Sn1 | 3.1950(9) | 2Rh1 | 2.8648(8) |
| Rh1–2Sn1 | 2.6880(7) | 1Ce | 3.333(1) | 1Sn1 | 3.080(1) |
| 1Sn4 | 2.692(1) | 2Sn4 | 3.5904(9) | 2Sn2 | 3.3384(9) |
| 1Sn2 | 2.742(1) | Sn2–1Rh1 | 2.742(1) | 2Sn4 | 3.3869(9) |
| 1Sn1 | 2.758(1) | 2Rh2 | 2.7792(8) | 2Sn1 | 3.5904(9) |
| 2Sn4 | 2.8648(8) | 1Rh2 | 2.801(1) | 2Sn3 | 3.6516(9) |
| 2Ce | 3.4783(9) | 1Sn3 | 2.984(1) | 1Ce | 3.696(1) |
| 1Ce | 3.712(1) | 2Ce | 3.2049(8) | 1Ce | 3.929(1) |
| Rh2–1Sn4 | 2.694(1) | 2Sn3 | 3.2524(9) | | |

Sn–Sn interactions range from 3.080(1) Å to 3.1950(9) Å. These values are significantly larger than the single-bond distance of 2.810 Å in the $\alpha$ modification of elemental Sn [31]. However, in view of the Sn–Sn distances in $\beta$-Sn [31] (4 × 3.02 Å; 2 × 3.18 Å) these contacts are also most likely bonding. There is no Rh–Rh interaction in the structure of $CeRh_2Sn_4$. The shortest Rh–Rh distance is about 4.40 Å, which is considerably longer than the Rh–Rh contacts of 2.68 Å in elemental rhodium [31].

Cerium atoms in the discussed structure have coordination number 18 with 7 Rh and 11 Sn atoms in their coordination shell. The six closest Ce–Sn contacts of 3.1681(8)–3.2049(8) Å are comparable with the sum of the atomic radii of Ce (1.82 Å) and Sn (1.41 Å) [32]. The nearest contact of Rh to Ce atom occurs at 3.4783(9) Å, which is much larger than the sum of their atomic radii: $r_{(Ce)} + r_{(Rh)} = 1.82$ Å + 1.34 Å = 3.16 Å.

The crystal structure of $CeRh_2Sn_4$ is closely related to that of $Ce_2Rh_3Sn_5$ ($Y_2Rh_3Sn_5$ structure type) [33], as illustrated in figure 2. In both these structures planar nets consisting of similar fragments occur. The close relationship between the $NdRh_2Sn_4$ and $Y_2Rh_3Sn_5$ type structures was also widely discussed in [13] and [34].

Both studied systems, $Ce_{1+x}Rh_2Sn_{4-x}$ and $La_{1+x}Rh_2Sn_{4-x}$, exhibit homogeneity ranges, as indicated by the changes in lattice parameters as well as good reproducible $x$ values derived from EDXS and WDXS analyses (see table 2). The DTA measurements revealed that the obtained compounds $RE_{1+x}Rh_2Sn_{4-x}$ do not melt below 1050 °C. In the following sections we focus on investigation of monocrystalline specimens of $CeRh_2Sn_4$ and the polycrystalline samples with $Ce_{1.2}Rh_2Sn_{3.8}$, $LaRh_2Sn_4$ and $La_{1.1}Rh_2Sn_{3.9}$ compositions.

### 3.2. XAS

The Ce $L_{III}$ XAS spectra for the sample $Ce_{1.2}Rh_2Sn_{3.8}$ (figure 3) show only a single 'white line' at an energy of ∼5723 eV. There is no evidence for additional peaks in the measured spectra, distributed analogously to the peaks observed in the spectrum for the $CeO_2$ standard. Thus one can conclude that Ce ions in the investigated system are exclusively in a trivalent state. Furthermore, there is no distinct difference between the spectra measured at 80 and 293 K. This indicates that the trivalent electronic configuration of Ce is stable in the examined temperature range.

### 3.3. RE core-level XPS spectra

Deeper insight into the character of the Ce 4f states in the systems $Ce_{1+x}Rh_2Sn_{4-x}$ ($0 \leqslant x \lesssim 0.2$) can be gained
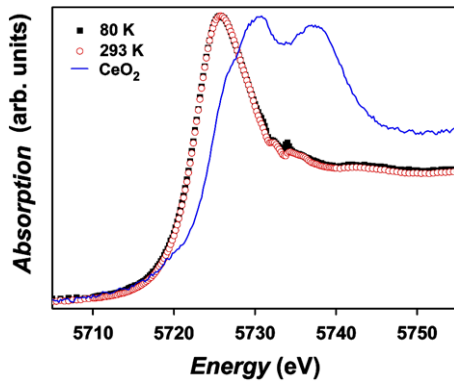
**Figure 3.** The x-ray absorption spectra of $Ce_{1.2}Rh_2Sn_{3.8}$ measured at temperatures of 80 and 293 K, in comparison to the $CeO_2$ standard.

from the Ce core-level XPS spectra. The detailed analysis has been restricted to the most intensive peaks related to the photoemission from Ce 3d and 4d states since the lifetime broadening of the other levels masks the fine structures originating from screening effects. For completeness, the XPS results for $CeRh_2Sn_4$ are analysed together with the corresponding spectra for the reference compound $LaRh_2Sn_4$.

The RE 3d XPS spectra of $CeRh_2Sn_4$, $Ce_{1.2}Rh_2Sn_{3.8}$ and $LaRh_2Sn_4$ (figure 4) consist of two sets of RE 3d photoemission lines due to the spin–orbit interaction. These lines originate from the $3d_{3/2}$ and $3d_{5/2}$ components of the final states and show a split of $\delta_{Ce} \approx 18.6$ eV or $\delta_{La} \approx 17.3$ eV, which is very similar to those obtained from the *ab initio* band structure calculations for the compounds $CeRh_2Sn_4$ and $LaRh_2Sn_4$ ($\delta_{Ce} \approx 18.83$ eV and $\delta_{La} \approx 17.22$ eV). Additionally, in the Ce 3d spectra there are slight contributions originating from the Sn 3s states at the binding energy of 885 eV, which overlap with the Ce 3d peaks. In turn, in the spectrum of $LaRh_2Sn_4$ there is a La MNN Auger line which forms a broad photoemission structure at a binding energy of ~866 eV.

Each set of RE 3d photoemission lines contains two contributions marked as $f^n$ and $f^{n+1}$, where $n = 0$ or 1 for La and Ce, respectively. The main peaks $f^n$ originate from a screening of the core hole by conduction electrons, whereas the $f^{n+1}$ satellites appear when the core hole becomes screened by an additional 4f electron owing to a $4f^n \rightarrow 4f^{n+1}$ transition during the photoemission process. The probability of transferring an electron to the exciton-like screening level centred on the core-ionized atom depends critically on its coupling to the other occupied states. Therefore the intensity of the $f^{n+1}$ contributions in the measured RE 3d XPS spectra reflects the degree of hybridization between the 4f and conduction band states in the initial state.

The main photoemission lines in the RE 3d XPS spectra ($f^n$) are wider for $CeRh_2Sn_4$ and $Ce_{1.2}Rh_2Sn_{3.8}$ than for the reference compound $LaRh_2Sn_4$. The observed broadening results from multiplet effects, which are absent in the La $f^0$ peaks, as well as a special broadening mechanism related to the so-called virtual-bound-state effects [35].

In the Ce and La 3d XPS spectra there are also distinct shoulders indicated in figure 4 by vertical arrows. The
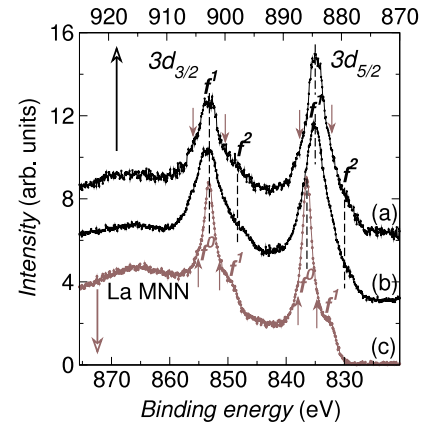


**Figure 4.** The RE 3d XPS spectra for $CeRh_2Sn_4$ (a), $Ce_{1.2}Rh_2Sn_{3.8}$ (b) and $LaR_2Sn_4$ (c). The $f^n$ and $f^{n+1}$ contributions are marked. Vertical arrows point to the shoulders originating from $Ce_2O_3$ or $La_2O_3$ in panels ((a), (b)) and (c), respectively.
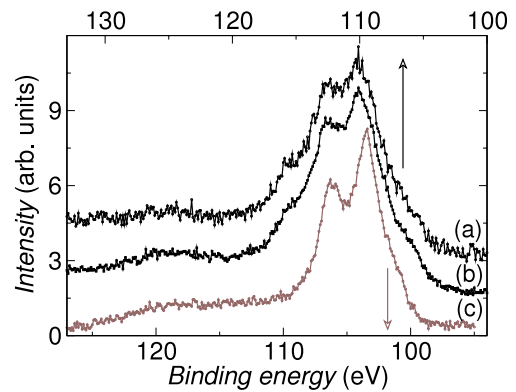


**Figure 5.** The RE 4d XPS spectra for the systems $CeRh_2Sn_4$ (a), $Ce_{1.2}Rh_2Sn_{3.8}$ (b) and $LaRh_2Sn_4$ (c).

comparative analyses of the Ce and La 3d XPS spectra recorded immediately after breaking samples and after some time clearly shows that these contributions were increasing with time. Since their energy positions correspond to the RE 3d photoemission lines of $Ce_2O_3$ [36] and $La_2O_3$ [37], respectively, these peaks can be assigned to surface oxidation.

There are no additional sharp peaks in the Ce 3d XPS spectra of $CeRh_2Sn_4$ and $Ce_{1.2}Rh_2Sn_{3.8}$ at a distance of ~11 eV from the $f^1$ photoemission lines which could be associated with the empty 4f shell in the final state. Thus we do not obtain evidence of a mixed valence of Ce. This finding is consistent with both the XAS spectra and the results of thermodynamic measurements.

The stable configuration of Ce ions has also been confirmed by the Ce 4d XPS spectra (figure 5), where one can see only a broad structure at binding energies ranging from 103 to 118 eV. These complexes originate from two sets of photoemission lines associated with the $4d^94f^n$ and $4d^94f^{n+1}$ final states, whose separation corresponds to the core hole 4d spin–orbit interaction: $\delta_{Ce} \approx 3.2$ eV and $\delta_{La} \approx 3.0$ eV. In the case of photoemission from Ce the detailed analysis of this region is not possible due to the strong exchange interaction between the photoemission holes and the 4f levels, which

causes complicated multiplet structures [38]. In the Ce 4d XPS spectra of $CeRh_2Sn_4$ and $Ce_{1.2}Rh_2Sn_{3.8}$ there are no additional sharp peaks at a binding energy of 118–124 eV, which could be attributed to $4d^9 4f^0$ final states and would provide evidence for an intermediate valence behaviour of Ce in the investigated systems. The weak broad features at a distance of 13 eV from the main photoemission lines are similar to those found in the La 4d XPS spectrum for $LaRh_2Sn_4$ and can be assigned to plasmon loss satellites. Analogous plasmon-like features were found in the RE 4d XPS spectra of the compounds $RERhSn_2$ [11] and $RE_3Rh_4Sn_{13}$ (RE = La or Ce) [39].

The quantitative analysis has been performed for the RE 3d XPS spectra based on the Gunnarsson and Schönhammer (GS) model [40, 41] in order to estimate the values of the parameter $\Delta$. This parameter describes the hybridization part of the Anderson impurity Hamiltonian and reflects the hybridization strength between the RE 4f and conduction band states. Details of the method have been described elsewhere [42]. The same procedure applied for all the investigated systems yielded the following values for the hybridization parameter $\Delta$ = 95 meV for $LaRh_2Sn_4$ and $\Delta$ = 80 meV for $CeRh_2Sn_4$ and $Ce_{1.2}Rh_2Sn_{3.8}$.

The estimated $\Delta$ values for $CeRh_2Sn_4$ and $Ce_{1.2}Rh_2Sn_{3.8}$ are smaller than the $\Delta$ value obtained for the reference compound $LaRh_2Sn_4$, which is in line with the general finding that hybridization tends to be smaller in Ce compounds than in their La counterparts due to the larger contraction of the 4f orbitals in Ce [41].

It is worthwhile to note that the estimated $\Delta$ values for the systems $CeRh_2Sn_4$ and $Ce_{1.2}Rh_2Sn_{3.8}$ are indistinguishable. Furthermore, there are no essential differences in shape and energy position of the photoemission lines in the Ce 3d and 4d XPS spectra of these compounds. These findings suggest that the character of the 4f states of the additional Ce atoms, which are intruded into the $CeRh_2Sn_4$ crystal structure, does not differ essentially from that of the Ce atoms occupying the 4c site. On the other hand, only about 17% of the Ce atoms could have different electronic structure. Besides, these additional Ce atoms may take up several nonequivalent sites in the crystal structure. Consequently, the XPS technique may not be sensitive enough to show such weak effects.

### 3.4. Specific heat

The overall temperature dependence of the specific heat for the compound $LaRh_2Sn_4$ is typical for a nonmagnetic metal (not shown). At ambient temperature the specific heat reaches the value of 175 J $(mol\,K)^{-1}$, which is in very good agreement with the estimate $C_p = 3nR \approx 174.6$ J $(mol\,K)^{-1}$, where $n$ is the number of atoms in the formula unit and $R$ denotes the gas constant (Dulong–Petit law).

Closer inspection of data for low temperatures reveals, however, that there is a distinct field dependence of the specific heat between about 3 K and about 13 K (figure 6). Such a behaviour hints at spin fluctuations. Indeed, the low temperature zero-field specific heat in this temperature range shows distinct deviation from the temperature dependence expected for nonmagnetic metals and can be well described by
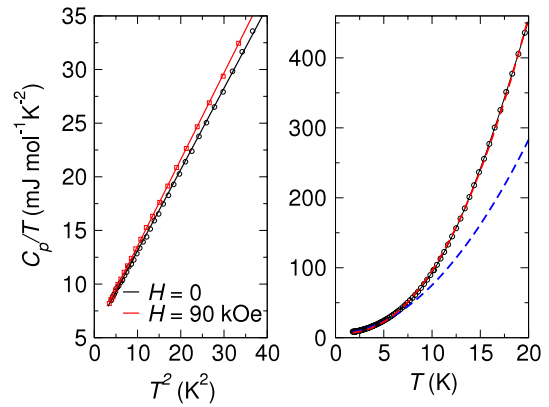


**Figure 6.** Low temperature specific heat of $LaRh_2Sn_4$ measured with and without an external magnetic field, plotted in a conventional $C_p/T$ versus $T^2$ presentation (left panel) or versus $T$ at $H = 0$, accompanied by fits to the equation $C_p/T = \gamma + \beta T^2$—dashed red (grey) line or equation (1)—dashed blue (dark grey) line (right panel).

using the following formula, in which the last term accounts for spin fluctuations [43]:

$$C_p = \gamma T + \beta T^3 + \delta^* T^3 \ln(T/T_{sf}). \tag{1}$$

The least-squares fit to the experimental data in a temperature range 2–20 K yields: $\gamma \approx 5.68$ mJ $(mol\,K^2)^{-1}$; $\beta \approx 0.69$ mJ $(mol\,K^4)^{-1}$; $\delta^* \approx 0.33$ mJ $(mol\,K^4)^{-1}$; $T_{sf} \approx 5.35$ K. The temperature dependence expected for nonmagnetic metals (equation (1) with $\delta^* = 0$) is followed only in a limited temperature range between 2 and 4 K with very similar values of the parameters $\gamma$ and $\beta$. Consequently, the Debye temperature $\theta_D$ can be estimated by using the formula $\beta = (12/5)Rn\pi^4\theta_D^{-3}$: $\theta_D \approx 270$ K. The obtained $\gamma$ value is related to the 'bare' Sommerfeld coefficient $\gamma_{bs}$ by the formula $\gamma = \gamma_{bs}(1+\lambda)$, in which $\lambda$ includes first of all electron–phonon and electron–magnon coupling constants. Since there is only a slight enhancement of the experimental $\gamma$ with respect to the $\gamma_{bs}$ derived from the electronic band structure calculations (see section 3.9), the mass renormalization is small and many-body effects are not dominant.

A similar behaviour of the low temperature specific heat has been found also for the system $La_{1.1}Rh_2Sn_{3.9}$ (not shown). For this system, however, the spin fluctuations are less pronounced.

For $CeRh_2Sn_4$, the specific heat data reveal a distinct anomaly with a maximum at $T_N = 3.2$ K, which points to magnetic ordering of the Ce moments. This ordering temperature coincides with the analysis of isothermal magnetization curves (section 3.6).

The application of an external magnetic field results first in an essential broadening of this peak and its shift towards lower temperatures due to the suppression of a magnetic ordering of the antiferromagnetic type. At higher fields (>15 kOe) the anomaly further broadens and shifts to higher temperatures with increasing magnetic field. Such a behaviour is typical for a Schottky anomaly caused by excitations between the Zeeman levels of the ground state doublet. The field dependence of
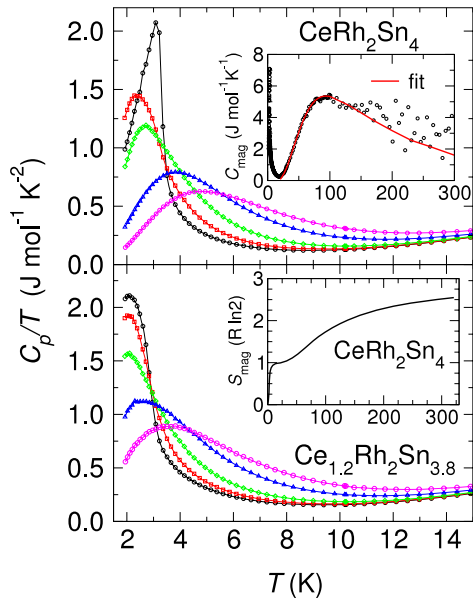
**Figure 7.** Low temperature specific heat divided by temperature $C_p/T$ for CeRh$_2$Sn$_4$ (upper panel) and for Ce$_{1.2}$Rh$_2$Sn$_{3.8}$ (lower panel) measured in different magnetic fields: pink (gray) ⊙—90 kOe; blue (dark gray) △—60 kOe; green (gray) ◇—30 kOe; red (gray) □—15 kOe; black ⊙—0. Upper inset shows the magnetic part of the specific heat $C_{mag}$ of CeRh$_2$Sn$_4$. Magnetic entropy for CeRh$_2$Sn$_4$ is presented in the inset of the lower panel. Below the measured temperature range the dependence $C_{mag}/T \sim T^2$ was assumed.

the Schottky anomaly obtained from the measurements on a number of small crystals is slightly different from that for the polycrystalline material (not shown), presumably due to anisotropy.

For the Ce$^{3+}$ ions in CeRh$_2$Sn$_4$ the crystal field is supposed to split the Hund's rule multiplet $^2$F$_{5/2}$ into three Kramer doublets due to the .*m*. point symmetry of the 4c site [44], which is occupied by Ce. To isolate the Ce 4f-derived part of the specific heat $C_{mag}(T)$ of CeRh$_2$Sn$_4$, the data for LaRh$_2$Sn$_4$ have been subtracted from the total specific heat of CeRh$_2$Sn$_4$, since the lattice contribution can be expected to be very similar for both CeRh$_2$Sn$_4$ and LaRh$_2$Sn$_4$. The resulting $C_{mag}(T)$ (inset of figure 7) shows a prominent broad feature with a maximum at about 90 K, which can be well described by a multi-Schottky anomaly resulting from thermally activated transitions from a ground state doublet to the higher-lying states. The best fit has been achieved assuming that the two excited doublets are separated from the ground state by the energy gaps $\Delta_1/k_B \approx 180$ K and $\Delta_2/k_B \approx 360$ K. It is worthwhile to stress that the specific heat in the analysed temperature range should be mostly unaffected by the spin fluctuation effects, which are visible only at lower temperatures.

Based on the magnetic specific heat, the entropy $S_{mag}(T)$ has been calculated. The results are presented in the lower inset of figure 7. At $T_N = 3.2$ K the entropy $S_{mag} \approx 0.65 R \ln 2$ is recovered, which is typical for three-dimensional magnets [45]. $S_{mag}(T)$ saturates at the value of $R \ln 2$ at a temperature of ∼13 K, indicating that a significant part of entropy is released through short-range magnetic correlations. At higher
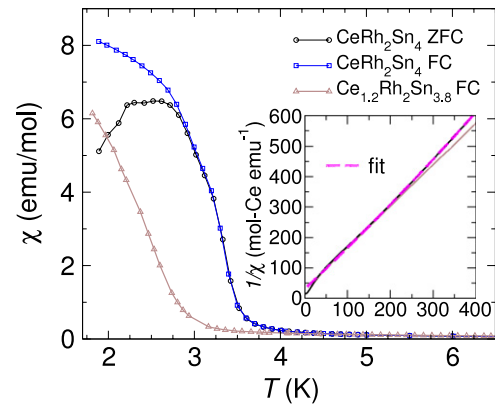


**Figure 8.** Low temperature static magnetic susceptibility data for CeRh$_2$Sn$_4$ and Ce$_{1.2}$Rh$_2$Sn$_{3.8}$ recorded in a magnetic field of 100 Oe in field-cooling (FC) and zero-field-cooling (ZFC) modes. The inset shows $1/\chi$ of CeRh$_2$Sn$_4$ and Ce$_{1.2}$Rh$_2$Sn$_{3.8}$ in a magnetic field of 70 kOe. The fit of the inverse susceptibility of CeRh$_2$Sn$_4$ by using the modified Curie–Weiss law covers the data above 200 K.

temperatures the magnetic entropy continues to increase and does not saturate up to ambient temperature, which is in line with the large crystal field splitting of the Ce $J = 5/2$ multiplet.

The specific heat and entropy do not indicate a Kondo effect in CeRh$_2$Sn$_4$. Consequently, the Kondo temperature for this system is low.

Finally, the effect of alloying is considered. As shown in figure 7, the specific heat of the sample Ce$_{1.2}$Rh$_2$Sn$_{3.8}$ shows a peak associated with the Ce magnetic ordering which is much broader than that for CeRh$_2$Sn$_4$ and shifted considerably towards lower temperatures. This result is in line with the magnetic susceptibility data discussed in section 3.5. The application of a magnetic field results in an essential broadening of this peak and, for fields stronger than about 30 kOe, leads to the shift of this anomaly towards higher temperatures due to the action of the Zeeman effect on the ground state doublet. It has to be noted that for a given magnetic field the Zeeman splitting is considerably smaller in Ce$_{1.2}$Rh$_2$Sn$_{3.8}$ than for CeRh$_2$Sn$_4$.

### 3.5. Static magnetic susceptibility

Figure 8 shows the static magnetic susceptibility for a set of single crystals of CeRh$_2$Sn$_4$ and a polycrystalline piece of Ce$_{1.2}$Rh$_2$Sn$_{3.8}$. For CeRh$_2$Sn$_4$ the magnetic susceptibility recorded at low magnetic fields (∼100 Oe) suggests a magnetic ordering. Detailed inspection of the data obtained in field-cooling and zero-field-cooling modes indicates that there are two humps at temperatures of 3.2 and 2.8 K, which may point to magnetic phase transitions. In the case of Ce$_{1.2}$Rh$_2$Sn$_{3.8}$ the feature in $\chi(T)$ related to the magnetic ordering is shifted considerably towards lower temperatures. The first kink, located at about 2.4 K, is very weak and the second hump is supposed to be shifted below 1.8 K. This indicates that inclusion of additional Ce atoms into the CeRh$_2$Sn$_4$ structure results in a distinct lowering of the magnetic ordering temperature.
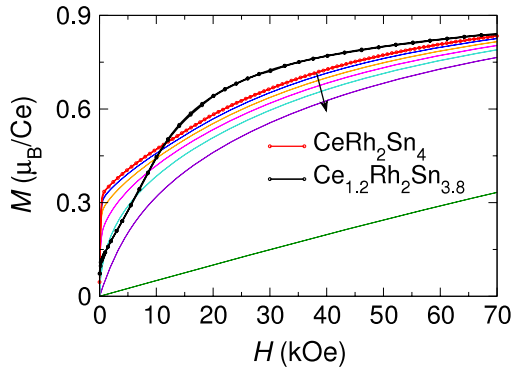
**Figure 9.** Magnetization versus external field for $CeRh_2Sn_4$ (coloured curves) and $Ce_{1.2}Rh_2Sn_{3.8}$ (black curve) measured at $T = 1.8$ K (thick lines) as well as at 2.2 K (blue), 2.6 K (orange), 3.0 K (pink), 3.4 K (light blue), 4 K (violet) and 15 K (green). The arrow indicates increasing temperature.



**Figure 10.** Arrott plot of isothermal magnetization curves of $CeRh_2Sn_4$. The demagnetization correction $H_{int} = H - 4\pi N M_{vol}$ for the factor $N = 0.19$ has been applied where $N$ was determined from the inverse slope of $M(H \to 0)$ at 1.8 K.

At high temperatures the magnetic susceptibility of both $CeRh_2Sn_4$ and $Ce_{1.2}Rh_2Sn_{3.8}$ does not depend on the applied magnetic field and can be well described by a modified Curie–Weiss law:

$$\chi = \chi_0 + \frac{C}{T - \theta}. \qquad (2)$$

The least-squares fits to the data in the temperature range of 200–400 K yield: $\chi_0 = -164 \times 10^{-6}$ emu mol$^{-1}$, $\theta = -22$ K and $C = 0.761$ emu K mol$^{-1}$ for $CeRh_2Sn_4$ and $\chi_0 = 7 \times 10^{-6}$ emu mol$^{-1}$, $\theta = -23$ K and $C = 0.879$ emu K mol$^{-1}$ for $Ce_{1.2}Rh_2Sn_{3.8}$. Thus, the effective Ce magnetic moment equals $\mu_{eff} = 2.47$ $\mu_B$/Ce in $CeRh_2Sn_4$ and $\mu_{eff} = 2.42$ $\mu_B$/Ce in $Ce_{1.2}Rh_2Sn_{3.8}$. These results are close to the value of 2.54 $\mu_B$/Ce expected for a free $Ce^{3+}$ ion, indicating that at high temperatures the magnetic moments of Ce ions in the investigated systems are localized and the other atoms do not carry magnetic moments. The significant negative $\theta$ values primarily results from the crystal electric field. The inclusion of additional Ce atoms leads only to the slight decrease of the average Ce effective moment and simultaneous increase of the paramagnetic Curie temperature, presumably due to the Kondo effect.

Below about 200 K, $1/\chi(T)$ of $CeRh_2Sn_4$ deviates from the Curie–Weiss-type straight lines which suggests a thermal depopulation of the excited crystal field levels associated with the $4f^1$ Ce ion (inset of figure 8). This observation coincides with the multi-Schottky anomaly in the magnetic specific heat observed at similar temperature (section 3.4).

The magnetic susceptibility of $LaRh_2Sn_4$ (not shown) is negative and shows only a slight temperature dependence. After correction for paramagnetic and ferromagnetic impurities, an extrapolation of $\chi(T)$ to $T = 0$ K results in $\chi_0 \approx -170 \times 10^{-6}$ emu mol$^{-1}$. For comparison, the sum of the diamagnetic increments for the closed-shell ions was calculated ($\chi_{dia}(Sn^{4+}) = -16 \times 10^{-6}$ emu mol$^{-1}$; $\chi_{dia}(La^{3+}) = -20 \times 10^{-6}$ emu mol$^{-1}$; $\chi_{dia}(Rh^{4+}) = -18 \times 10^{-6}$ emu mol$^{-1}$ [46]). Such an estimation gives the value of $-120 \times 10^{-6}$ emu mol$^{-1}$, which is less than the obtained $\chi_0$ value. This indicates that $LaRh_2Sn_4$ is more strong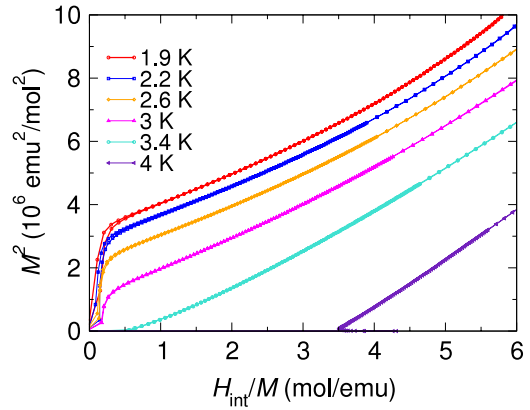ly diamagnetic than one could expect based on the independent electron description. In turn, for $La_{1.1}Rh_2Sn_{3.9}$ the extrapolated value of $\chi(T)$, after correction for the impurities, equals about $-143 \times 10^{-6}$ emu mol$^{-1}$. This indicates weaker diamagnetic properties of the nonstoichiometric system.

### 3.6. Isothermal magnetization

Figure 9 displays isothermal magnetization curves for $CeRh_2Sn_4$ plotted as a function of external magnetic field. The data recorded with increasing and decreasing field do not show distinct hysteresis. The $M(H)$ curves recorded at temperatures below $T_N$ exhibit a shoulder at about 1.5 kOe. The overall shape of the curve for the lowest accessible temperature of 1.8 K is typical for noncollinear (canted) antiferromagnet or strong single-ion anisotropy. The observed crooking in the $M(H)$ curves gradually washes out upon increasing temperature and vanishes at about 3.4 K. At higher temperatures the $M(H)$ curves are consistent with paramagnetic Ce ions. For the highest available field of 70 kOe the magnetic moment of Ce reaches a value of 0.83 $\mu_B$/Ce at 1.8 K and does not saturate. An extrapolation of $M(1/H)$ to $1/H = 0$ yields 0.98 $\mu_B$/Ce, much less than the moment $gJ = 2.14$ $\mu_B$ for the free $Ce^{3+}$ ions, which is due to the well-isolated doublet ground state.

In order to get further insight into the magnetic ground state properties of $CeRh_2Sn_4$, the isothermal $M(H)$ curves were corrected for demagnetization effect and re-plotted as $M^2$ against $H_{int}/M$ (figure 10). The obtained Arrott plots show that the magnetic ordering temperature is slightly above 3 K, which is consistent with the specific heat data (section 3.4). There is a spontaneous magnetization below $T_N$ which equals about 0.31 $\mu_B$/Ce at 1.8 K and decreases with increasing temperature.

For the sample $Ce_{1.2}Rh_2Sn_{3.8}$ the isothermal magnetization at $T = 1.8$ K (figure 9) shows a smaller increase at low magnetic fields, which points to a weaker ferromagnetic component of the ordered state. An estimate based on the Arrott plot gives only a small spontaneous magnetic moment of about 0.12 $\mu_B$/Ce at 1.8 K (estimated according to the procedure

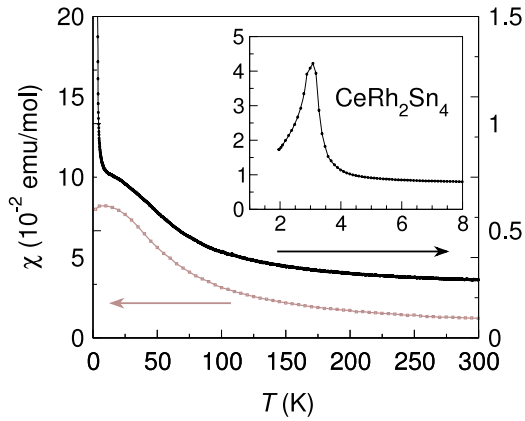**Figure 11.** Dynamic magnetic susceptibility of CeRh$_2$Sn$_4$ (black) and LaRh$_2$Sn$_4$ (grey).



**Figure 12.** Resistivity of polycrystals CeRh$_2$Sn$_4$ (black), Ce$_{1.2}$Rh$_2$Sn$_{3.8}$ (green, triangle) and the reference systems LaRh$_2$Sn$_4$ (red, circle) and La$_{1.1}$Rh$_2$Sn$_{3.9}$ (grey, square). Inset shows the comparison of the low temperature resistivity of CeRh$_2$Sn$_4$ and Ce$_{1.2}$Rh$_2$Sn$_{3.8}$ (the data were shifted along the vertical axis). For clarity, only every 20th experimental point has been drawn.

given in the description of figure 10, assuming $N = 0.88$). For $H_{ext} = 70$ kOe the magnetic moment of Ce reaches a value similar to that observed for the compound CeRh$_2$Sn$_4$ (0.83 $\mu_B$/Ce) and also does not saturate.

### 3.7. Dynamic magnetic susceptibility

Further insight into the magnetic properties of the systems RERh$_2$Sn$_4$ can be gained from the dynamic magnetic susceptibility (figure 11). For both CeRh$_2$Sn$_4$ and LaRh$_2$Sn$_4$ the temperature dependence of $\chi_{ac}$ reveals a broad peak centred at about 17 K and 13 K, respectively. Such features hint at spin fluctuation effects, presumably related to the Rh 4d electrons, as was proposed previously for the compounds CeRhSn [10] and RERhSn$_2$ (RE = Ce or La) [11].

In addition, in the case of CeRh$_2$Sn$_4$ the recorded $\chi_{ac}(T)$ shows a peak at about 3.1 K (the inset of figure 11), giving evidence for a magnetic phase transition. This result is consistent with the specific heat, which revealed a magnetic ordering in CeRh$_2$Sn$_4$ at a very similar temperature (section 3.4).

### 3.8. Electrical resistivity

Figure 12 shows the temperature dependence of the electrical resistivity $\rho(T)$ of CeRh$_2$Sn$_4$, Ce$_{1.2}$Rh$_2$Sn$_{3.8}$ and the reference systems LaRh$_2$Sn$_4$ and La$_{1.1}$Rh$_2$Sn$_{3.9}$. The resistivity of the compounds Ce$_{1.2}$Rh$_2$Sn$_{3.8}$ and La$_{1.1}$Rh$_2$Sn$_{3.9}$ is significantly larger than those of the compounds RERh$_2$Sn$_4$ and (RE = La, Ce) and shows much weaker temperature dependence, which indicates a substantial amount of disorder in the nonstoichiometric samples.

LaRh$_2$Sn$_4$ exhibits a metallic behaviour in the whole investigated temperature range (figure 12). The low temperature part of $\rho(T)$ does not follow a $T^5$ dependence (phonon scattering), presumably due to the spin fluctuation effects. At higher temperatures there is also a significant deviation from the behaviour which one would expect based on the Bloch–Grüneisen description. The weak shoulder around 150 K could be assigned to interband s–d scattering of the conduction electrons [47], which is often observed for intermetallic compounds with transition metal atoms.
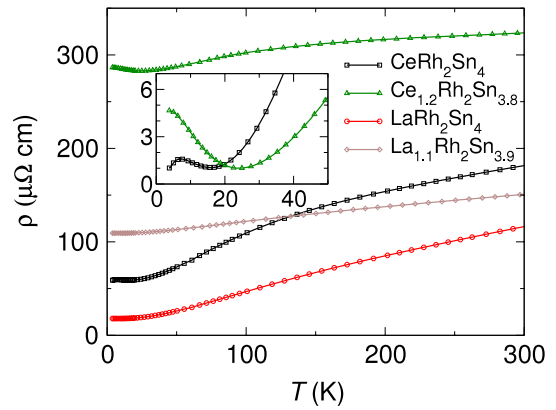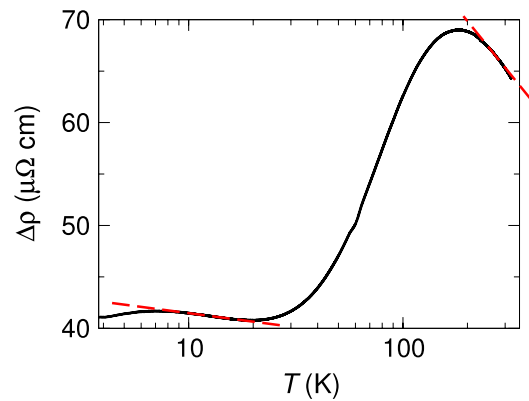


**Figure 13.** Magnetic part of the resistivity $\Delta\rho$ of CeRh$_2$Sn$_4$. Red dashed lines indicate the temperature ranges in which $\Delta\rho \sim \ln(T)$.

The resistivity for CeRh$_2$Sn$_4$ shows a more complex temperature dependence with a weak minimum at about 17 K and a pronounced shoulder around about 130 K (figure 12). At higher temperatures, $\rho(T)$ increases almost linearly and reaches a value of about 180 $\mu\Omega$ cm at 300 K. Such a shape of the resistivity curve is typical for the compounds in which Kondo interactions coexist with crystal field effects [48].

In order to get a deeper insight into the electron scattering mechanisms in CeRh$_2$Sn$_4$, the Ce 4f-derived part of the resistivity is estimated on the assumption that the lattice contribution is given by $\rho(T)$ of the nonmagnetic isostructural compound LaRh$_2$Sn$_4$. The difference curve $\Delta\rho(T)$ is presented in figure 13. The magnetic part of resistivity $\Delta\rho(T)$ shows two logarithmic slopes which, based on the Cornut–Coqblin theory [48], can be assigned to the incoherent Kondo scattering of conduction electrons on the crystal field levels of the $J = 5/2$ multiplet of Ce$^{3+}$ ions. Thus a broad maximum in $\Delta\rho(T)$ at $T \approx 100$ K can be associated with the overall crystal field splitting of the ground state multiplet, in agreement with the magnetic specific heat $C_{mag}$ (section 3.4). The least-squares

**Table 5.** Structural data obtained from the LDA calculations for the compounds $CeRh_2Sn_4$ and $LaRh_2Sn_4$. All atoms are located at 4c sites ($x$, 1/4, $z$). The calculated lattice parameters and atomic coordinates were rounded to two and three significant digits, respectively.

| Compound: | $CeRh_2Sn_4$ | | $LaRh_2Sn_4$ | |
|---|---|---|---|---|
| $a$ (Å) | 18.26 | | 18.37 | |
| $b$ (Å) | 4.47 | | 4.50 | |
| $c$ (Å) | 7.08 | | 7.13 | |
| $V$ (Å$^3$) | 577.89 | | 589.40 | |
| | Atomic coordinates | | | |
| Atom | $x$ | $z$ | $x$ | $z$ |
| RE | 0.3579 | 0.0023 | 0.3583 | 0.0034 |
| Rh1 | 0.0359 | 0.7483 | 0.0351 | 0.7511 |
| Rh2 | 0.2857 | 0.5173 | 0.2859 | 0.5176 |
| Sn1 | 0.0316 | 0.3634 | 0.0318 | 0.3626 |
| Sn2 | 0.1830 | 0.8017 | 0.1829 | 0.8038 |
| Sn3 | 0.1941 | 0.2221 | 0.1934 | 0.2214 |
| Sn4 | 0.4319 | 0.4877 | 0.4319 | 0.4807 |

fitting of the $\Delta\rho(T)$ data to the Kondo formula

$$\Delta\rho(T) = \rho'_0 - c_k \ln T, \qquad (3)$$

for the two temperature ranges 8–21 K and 230–280 K yields the following values of the parameter $\rho'_0$ and the Kondo coefficient $c_k$: $c_{k1} \approx 1.1\ \mu\Omega$ cm K$^{-1}$, $\rho'_{01} \approx 43.9\ \mu\Omega$ cm for $8\ \mathrm{K} \leqslant T \leqslant 20\ \mathrm{K}$; $c_{k2} \approx 11.0\ \mu\Omega$ cm K$^{-1}$, $\rho'_{02} \approx 127.8\ \mu\Omega$ cm for $225\ \mathrm{K} \leqslant T \leqslant 300\ \mathrm{K}$. The rather small value of $c_k$ for the ground crystal field doublet hints at only slightly enhanced DOS at the Fermi level in $CeRh_2Sn_4$. The minimum in the resistivity curves becomes deeper and shifts towards higher temperatures if one substitutes additional Ce atoms into the $CeRh_2Sn_4$ structure. Thus, for the compound $Ce_{1.2}Rh_2Sn_{3.8}$, the Kondo scattering is supposed to be considerably stronger than for the compounds $CeRh_2Sn_4$. In turn, the deviation of the resistivity of $CeRh_2Sn_4$ from logarithmic behaviour at low temperatures could be assigned to correlations between Ce ions, which develop above the magnetic ordering temperature and are expected to reduce the Kondo scattering.

### 3.9. Electronic band structure calculations

First, a full computational structure optimization was performed for both $LaRh_2Sn_4$ and $CeRh_2Sn_4$ based on the electronic band structure calculations within the LDA approximation. The experimental lattice parameters and atomic positions for the compound $CeRh_2Sn_4$ (tables 1 and 3) were taken as starting points. The results are listed in table 5. The atomic coordinates derived from the FPLO calculations were cross-checked using the Wien2k computer code [22], where the atomic forces were calculated according to the method proposed by Yu *et al* [49]. For the optimized atomic positions the total forces on each atom were smaller than 5 mRyd/au. Furthermore, the theoretical data for $CeRh_2Sn_4$ are in good agreement with the experimental ones (table 3) and do not differ essentially from those estimated for the compound $LaRh_2Sn_4$. Nevertheless, single-crystal diffraction
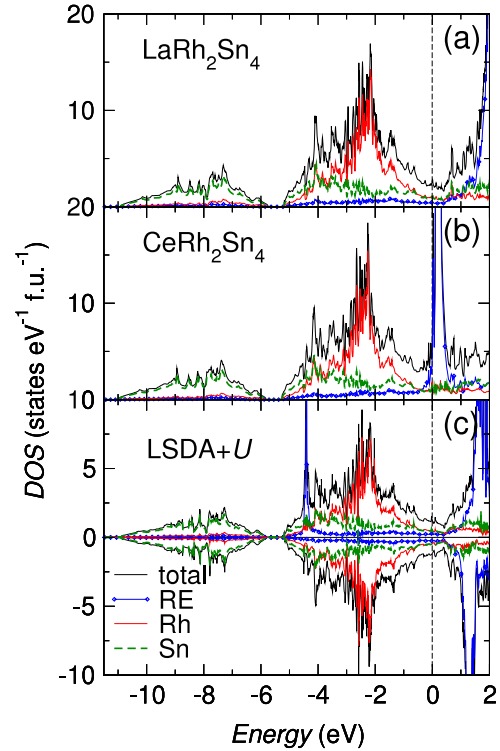


**Figure 14.** The total (black lines) and atomic resolved (blue-RE; red-Rh; green-Sn) DOSs for the compounds $LaRh_2Sn_4$ (a) and $CeRh_2Sn_4$ ((b), (c)) calculated within the LDA approximation ((a), (b)) and using the LSDA + $U$ ($U = 6$ eV; $J = 0$ eV) approach applied for the Ce 4f shell. The common vertical dashed line indicates the position of the Fermi level.

studies of $LaRh_2Sn_4$ are still needed to verify unequivocally the theoretical estimates.

The calculated lattice parameters are in good agreement with the experimental ones for both $CeRh_2Sn_4$ and $LaRh_2Sn_4$. The slight differences, similar for both systems, can be understood as due to the tendency of the LDA approximation to overbind. This suggests that the Ce 4f states do not contribute significantly to the chemical bonding in $CeRh_2Sn_4$.

Figure 14 shows the total and partial atomic resolved DOSs obtained for the compounds $CeRh_2Sn_4$ and $LaRh_2Sn_4$ within the LDA approximation. Spin-polarized band structure calculations have also been performed and revealed a magnetic ground state for $CeRh_2Sn_4$. In contrast, for the reference compound $LaRh_2Sn_4$ the calculations yielded a nonmagnetic ground state. The theoretical results show that only the Ce atoms carry magnetic moments in the investigated systems (table 6). The calculated spin moments of Rh and Sn are very small in $CeRh_2Sn_4$ (below 0.005 $\mu_B$), while in $LaRh_2Sn_4$ spin polarization is not observed. The calculated values of the DOS at the Fermi level and the 'bare' values of Sommerfeld coefficients $\gamma_{bs}$ for both $CeRh_2Sn_4$ and $LaRh_2Sn_4$ are listed in table 6.

The spectroscopic results (sections 3.2 and 3.3) as well as the thermodynamic data (sections 3.4, 3.5, and 3.8) unanimously indicate a stable trivalent state of Ce ions in $CeRh_2Sn_4$, suggesting the strongly correlated character of the Ce 4f states. In contrast, in the L(S)DA calculations the partial

**Table 6.** DOS ($E_F$), the 'bare' values of a Sommerfeld coefficient $\gamma_{bs}$ and Ce spin moments $\mu_{spin}$ calculated for $CeRh_2Sn_4$ and $LaRh_2Sn_4$ within different approximations for the XC potential.
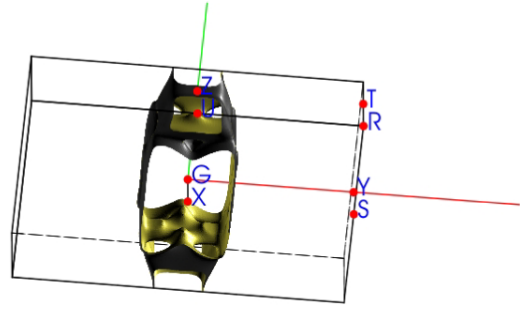
| | | | | $LaRh_2Sn_4$ |
|---|---|---|---|---|
| | | | $CeRh_2Sn_4$ | |
| | | | LSDA + U | |
| | LDA | LSDA | ($U_{eff}$ = 6 eV) | LDA |
| DOS ($E_F$) (states eV$^{-1}$ f.u.$^{-1}$) | 6.63 | 6.16 | 2.01 | 2.12 |
| $\gamma_{bs}$ (mJ mol$^{-1}$ K$^{-2}$) | 15.6 | 14.5 | 4.7 | 5.0 |
| $\mu_{spin}$ ($\mu_B$) | — | 0.22 | 1.01 | — |

Ce 4f DOS forms an unrealistic peak at the Fermi level due to the large underestimation of the Coulomb repulsion of the f electrons in this approximation. In order to account for the strong Coulomb interaction within the Ce 4f shell, additional band structure calculations using the LSDA+U approach have been carried out (figure 14). Inclusion of the Hubbard-type correlation term $U$ to the exchange–correlation potential shifts the occupied Ce 4f band towards higher binding energy and the unoccupied 4f states above the Fermi level. Consequently, it removes the incorrect hybridization with conduction states and yields the qualitatively correct physical picture of $Ce^{3+}$ states for the $U$ values larger than ~3.5 eV. Then, the Ce spin moment equals about 1 $\mu_B$ and the occupied and unoccupied Ce 4f states show a split of the order of $U$.

The variation of the $U$ and $J$ parameters in the physically reasonable ranges of 3.5–8 eV and 0–0.7 eV, respectively, results mainly in a shift of the occupied Ce 4f states on the energy scale. The shape of the electronic DOS for all atoms except Ce is almost independent of the choice of $U$ and $J$ (in the investigated range), which justifies the application of the LSDA + U approach.

The calculations within the LSDA + U approximation with $U = 6$ eV (typical for Ce in a trivalent state [50]) results in magnetic spin moments on Rh and Sn smaller than 0.01 $\mu_B$. Hence, in a first approximation, magnetic ordering in $CeRh_2Sn_4$ can be explained as due to the RKKY-type interactions between the rather localized Ce 4f states. The ferromagnetic and several possible antiferromagnetic spin arrangements were studied by means of calculations for magnetic supercells. Since some of the antiferromagnetic solutions have deeper energy than the ferromagnetic one, antiferromagnetic couplings are dominating in the investigated system. The analysis of the band structure (not shown) reveals that the main dispersion is along the crystallographic $y$ axis, suggesting that this is the primary direction of magnetic interactions in $CeRh_2Sn_4$. The presence of frustration of magnetic interactions in the compound provides an additional mechanism for noncollinearity. Further experimental studies, for instance neutron scattering measurements, should be performed in order to determine the magnetic structure of $CeRh_2Sn_4$ at low temperatures.

The shape of all partial DOSs, except for the 4f states, is very similar for $LaRh_2Sn_4$ and $CeRh_2Sn_4$ with the Ce 4f shell treated using the LSDA + U approach. Furthermore, the band structure in the vicinity of $E_F$ as well as the residual tiny 4f contribution to the calculated DOS in a region of the low



**Figure 15.** Selected sheet of the Fermi surface of $LaRh_2Sn_4$. The high symmetry points are labelled according to the standard notation.

binding energies are nearly the same for $CeRh_2Sn_4$ (LSDA + U approximation) as for the reference compound $LaRh_2Sn_4$. These findings support the picture that the Ce 4f states in $CeRh_2Sn_4$ are localized and the RKKY-type interactions between the local 4f moments determine the magnetic ground state properties of this compound.

Finally, it is of interest to get an insight into the possible origin of the spin fluctuations on Rh in both $LaRh_2Sn_4$ and $CeRh_2Sn_4$, which are suggested by the dynamic magnetic susceptibility and specific heat data. Even for the compound $CeRh_2Sn_4$ the band structure results did not show any localized magnetic moment for the Rh atoms. Further, the numerically calculated Rh DOS ($E_F$) is smaller than one state per eV and atom. A crude estimate (assuming the exchange integral for Rh 4d states to be of the order of 0.5) shows that the Stoner criterion for band magnetism is not fulfilled. Fixed spin moment calculations for $LaRh_2Sn_4$ also do not give evidence for ferromagnetic spin fluctuations in this compound. In order to investigate in detail indications of magnetic instabilities, the Fermi surface was analysed. Since the bands in the vicinity of $E_F$ are very similar for both $CeRh_2Sn_4$ (within the LSDA + U approximation) and $LaRh_2Sn_4$, these two systems have topologically identical Fermi surfaces. Therefore only the results for the compound $LaRh_2Sn_4$ are presented.

The Fermi surface of the compound $LaRh_2Sn_4$ consists of seven sheets. The most interesting features of the Fermi surface are the parallel 'pieces' of the sheets shown in figure 15, which could generate 'nesting' instabilities. Since there is a significant contribution of both Rh1 and Rh2 states to these Fermi surface sections, the observed nesting features might be the origin for the spin fluctuations suggested by the measurements.

### 3.10. Chemical bonding

The chemical bonding was investigated by analysis of the electron localizability indicator in combination with the electron density.

The same topology of the charge density has been found for $CeRh_2Sn_4$ and $LaRh_2Sn_4$ based on the electronic band structure calculations within the LDA approximation and using the LSDA + U ($U = 6$ eV) approach for the Ce 4f states, respectively. This is in line with the very similar band

structures of these compounds. The only difference between the results obtained for $CeRh_2Sn_4$ and $LaRh_2Sn_4$ occurs at the RE sites and originates from the 4f electron density localized on the Ce atoms.

For $LaRh_2Sn_4$, the evaluation of the electron density according to the QTAIM method of Bader [30] yielded an atomic basin for each atom. Integration of the electron density within the atomic basins gives 54.30 electrons per La, $45.65e^-$ per Rh (on average) and $50.35e^-$ per Sn (on average). In this way the whole electron density is distributed in the basins centred at the atomic nuclei. The result reflects the charge difference between the interacting atomic volumes. The so-obtained QTAIM charges and the charge transfer giving the ionic charges of $+2.7$ for La, $-0.35$ for Sn and $-0.65$ for Rh are in agreement with the electronegativity relation between the components ($EN_{La} < EN_{Sn} < EN_{Rh}$). Interestingly, the deviations from the average for individual sites are quite large, especially for tin atoms. So, for the Sn1 and Sn4 position even less than 50 electrons were found. This makes these sites attractive for replacement by more electropositive elements and might explain the formation of the homogeneity ranges for the $RE_{1+x}Rh_2Sn_{4-x}$ phases.

The bonding situation was further analysed utilizing the electron localizability indicator (ELI-D). A marked feature of the ELI-D distribution in $LaRh_2Sn_4$ are the spherical regions of high ELI-D values around the atomic nuclei, visualizing the atomic shell structure (figure 16, top). The penultimate ELI-D shells of Rh (fourth shell) and La (fifth shell) are structurized, i.e. deviate from the spherical symmetry characteristic for non-interacting isolated atoms, which was shown to be an indication for participation of these electrons in the bonding [51, 52].

The next relevant topological feature are the ELI-D maxima between the Sn and Rh atoms forming pentagonal prisms centred by the La atoms (figure 16, bottom). They can be seen as a signature of the covalent bonding between tin and rhodium atoms. All together, the Rh and Sn atoms form a network polyanion with covalent bonds. The possible polar character of these bonds is characterized by the charge transfer between the QTAIM atoms (see above). Lanthanum species are located in the cavities of the polyanion.

The attractors of Rh–Sn bonds are shifted from the middle point of the shortest contact toward La. Their basins have common borders not only with Rh and Sn core basins, as it should be for the two-centre bond, but also with the core basin of lanthanum, indicating its participation in these bonds.

In total, chemical bonding in $LaRh_2Sn_4$ may be described by the formation of an $[Rh_2Sn_4]^{2.7-}$ polyanion by Sn–Sn and Sn–Rh bonds. Lanthanum shows two types of interactions with the polyanion: one is more of ionic nature with a charge transfer, while the second one is a directed one caused by participation of the electrons of the fifth shell of lanthanum in the bonding.

### 3.11. XPS valence band spectra

Figure 17 shows the XPS valence band spectra of $CeRh_2Sn_4$ and $LaRh_2Sn_4$. The detailed analysis of the experimental data
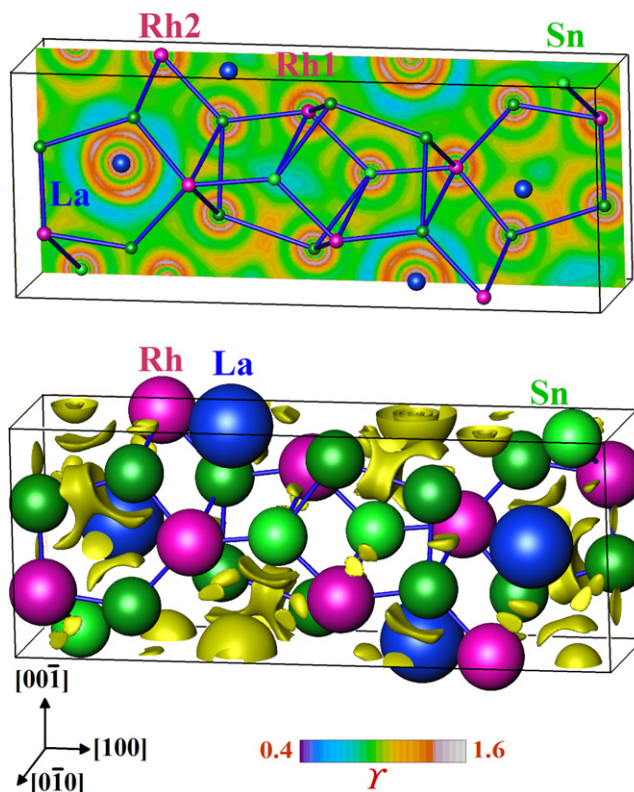


**Figure 16.** Electron localizability indicator $\Upsilon$ in $LaRh_2Sn_4$: (top) ELI-D map at $y = 0.25$ showing the structuring of the penultimate shells of rhodium and lanthanum; (bottom) isosurface of ELI-D with $\Upsilon = 1.030$ visualizing the positions of the ELI-D attractors in the $[Rh_2Sn_4]$ polyanion and their shift from the Rh–Sn and Sn–Sn contacts caused by the participation of lanthanum in the covalent interaction with the polyanion: the atomic spheres are enlarged to cover the inner shells of the atoms for clarity.

has been carried out using the theoretical XPS spectra, which were estimated based on the partial DOSs obtained within the LSDA approximation and using the LSDA $+ U$ ($U = 6$ eV) approach for the Ce 4f states (see section 2.2). The background estimated according to the Tougaard algorithm [53] has been subtracted from the experimental spectra.

The main peak in the valence band spectra, located at a binding energy of $\sim$2.5 eV, originates mainly from the Rh 4d states hybridized with the Sn 5p states. The second peak centred at about 8 eV is related to photoemission from the Sn 5s states.

The theoretical simulation reproduces well the overall shape of the XPS valence band spectra for both compounds. The slight distinction between the calculated and measured intensity in the vicinity of $E_F$ is similar for both $CeRh_2Sn_4$ and $LaRh_2Sn_4$ and is supposed to originate from the inadequacy of the atomic-like photoemission cross sections for the valence band states, as often observed for Ce- and La-based intermetallics [39, 54]. In turn, the slight discrepancy in peak positions between the experimental and the calculated XPS valence band spectra is presumably associated with the incomplete screening of the photoemission holes, which cannot be described by a ground state calculation. This effect leads to a slightly smaller kinetic energy of the emitted
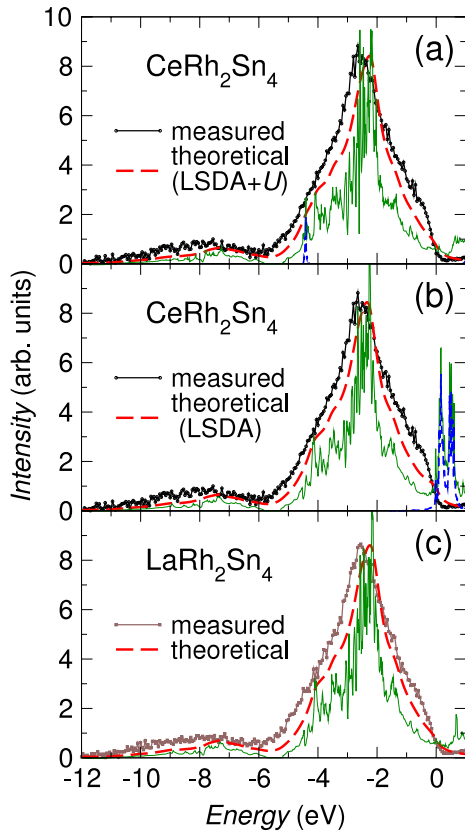
**Figure 17.** Comparison of the experimental XPS valence band spectra of $CeRh_2Sn_4$ and $LaRh_2Sn_4$ (background subtracted) with those calculated based on the partial DOSs obtained within the LDA approximation and using the LSDA + $U$ ($U = 6$ eV; $J = 0$ eV) approach for the Ce 4f states. The thin (green) solid lines represent the sum of the partial $l$-resolved DOSs multiplied by the corresponding cross sections [20]. The thin dashed (blue) lines show the partial Ce 4f DOSs multiplied by the photoemission cross section [20].



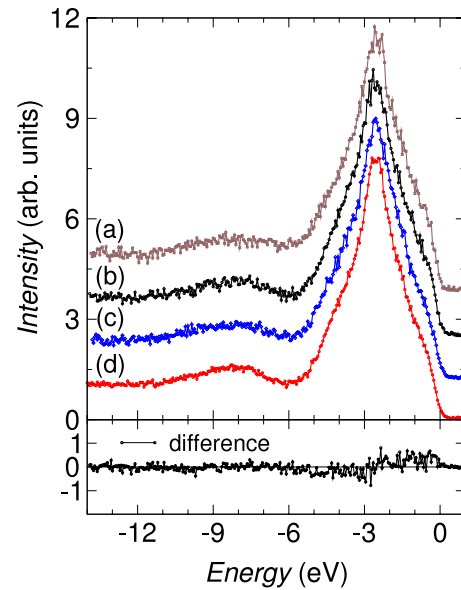**Figure 18.** The XPS valence band spectra of $Ce_{1.2}Rh_2Sn_{3.8}$ (a), $CeRh_2Sn_4$ (b), $LaRh_2Sn_4$ (c) and $La_{1.1}Rh_2Sn_{3.9}$ (d). Lower panel shows that there is no significant difference between the spectra of $CeRh_2Sn_4$ and $LaRh_2Sn_4$.

photoelectrons and consequently to a tiny shift of the measured XPS peaks towards higher binding energies [55].

In order to illustrate the magnitude of the Ce 4f contributions to the XPS valence band spectra, the partial Ce 4f DOSs as well as the sum of all partial $l$-resolved DOSs, multiplied by the corresponding cross sections, are plotted in figure 17. It is clearly visible that photoemission from the 4f states should give only a small contribution to the measured spectra, as compared to the other valence band states. Therefore the XPS valence band spectra cannot give unequivocal information about the Ce 4f states in $CeRh_2Sn_4$.

Direct comparison of the $CeRh_2Sn_4$ and $LaRh_2Sn_4$ XPS valence band spectra (figure 18) shows that the differences between these spectra are smaller than the experimental noise. This gives further support for the localized character of the Ce 4f states in $CeRh_2Sn_4$ since the electronic band structure calculations revealed very similar DOSs and band structures for $CeRh_2Sn_4$ (within the LSDA + $U$ approximation) and $LaRh_2Sn_4$, except for the Ce 4f bands.

There is also no distinct difference between the XPS valence band spectra for $CeRh_2Sn_4$ and $Ce_{1.2}Rh_2Sn_{3.8}$ as well as between the spectra for $LaRh_2Sn_4$ and $La_{1.1}Rh_2Sn_{3.9}$

(figure 18). This is expected because the XPS valence band spectra are dominated by the Rh 4d states. Consequently, the slight differences in small contributions to the measured spectra cannot be clearly detected.

## 4. Discussion

The performed experimental studies show that at room temperature the Ce ions in $CeRh_2Sn_4$ are in a trivalent state and the system behaves like an ordinary paramagnet with the full moment expected for $Ce^{3+}$ ions. At lower temperatures, the crystal field splitting of the $J = 5/2$ multiplet becomes important. The best description of the specific heat data has been achieved with two excited Kramers doublets separated from the ground state doublet by the energy gaps $\Delta_1/k_B \approx 180$ K and $\Delta_2/k_B \approx 360$ K. Although there is evidence for the Kondo effect in the resistivity data, the Kondo temperature of $CeRh_2Sn_4$ is supposed to be low.

$CeRh_2Sn_4$ orders magnetically at 3.2 K. The magnetic susceptibility and magnetization curves indicate that the ground state magnetic structure is of a noncollinear antiferromagnetic type. The electronic band structure calculations confirmed a magnetic ground state of $CeRh_2Sn_4$ and revealed significant magnetic moments only at the Ce sites, whereas all the Rh and Sn atoms were nearly unpolarized. Hence, in a first approximation, magnetic ordering in $CeRh_2Sn_4$ is explained as due to the RKKY-type interactions between the localized Ce 4f moments. The strongest magnetic interactions are expected along the $y$ axis. In addition, the dynamic magnetic susceptibility curve for $CeRh_2Sn_4$ shows a broad maximum centred at about 17 K. A similar feature has been found for the reference compound $LaRh_2Sn_4$ at a temperature of 13 K and has been interpreted in

terms of the spin fluctuation effect due to the Rh 4d electrons. The presence of spin fluctuations has also been confirmed by the low temperature specific heat data. The Fermi surface analysis has shown that there are some parallel sections of the sheets, which might generate 'nesting' instabilities in both $CeRh_2Sn_4$ and $LaRh_2Sn_4$ and be responsible for the spin fluctuation effects. Further experimental studies, for instance neutron scattering experiments, should be performed in order to gain a deeper insight into the magnetic properties of $CeRh_2Sn_4$.

The analysis of charge density maps as well as the computational crystal structure optimization excluded a significant contribution of the Ce 4f states to the chemical bonding in $CeRh_2Sn_4$. This finding is consistent with the recorded Ce $L_{III}$ XAS and core-level XPS spectra, which point to a trivalent configuration of Ce. Furthermore, the band structure in the vicinity of the Fermi level as well as the residual tiny 4f contribution to the calculated DOS in a region of the low binding energies were found to be nearly the same for $CeRh_2Sn_4$ (LSDA + $U$ approximation) as for the reference compound $LaRh_2Sn_4$. This supports a localized character of the Ce 4f states in $CeRh_2Sn_4$. Nevertheless, the RE 3d XPS spectra point to the significant hybridization between the RE 4f and conduction band states. The hybridization parameter $\Delta$ estimated based on the Gunnarsson–Schönhammer model calculations equals about 80 meV for $CeRh_2Sn_4$ and about 95 meV for $LaRh_2Sn_4$.

The investigations indicate that $CeRh_2Sn_4$ as well as $LaRh_2Sn_4$ exhibit homogeneity ranges, which explains the distinct discrepancies in lattice parameters between the data obtained here and those previously reported [13]. The EDXS and WDXS studies reveal that the investigated systems can be described using the formula $RE_{1+x}Rh_2Sn_{4-x}$, where $0 \leqslant x \lesssim 0.2$ for Ce and $0 \leqslant x \lesssim 0.1$ in the case of La. At present we cannot propose a reasonable model to describe the substitution of rare-earth atoms into the $RERh_2Sn_4$ structure. The replacement of Sn atoms in one crystallographic site by RE atoms seems to be not likely from the point of view of the calculated charge density maps. Further studies of crystal structures of the compounds $RE_2Rh_3Sn_5$ and $RE_{1+x}Rh_2Sn_{4-x}$ (RE = Ce, La) using single-crystal refinements as well as transmission electron microscopy are required.

The electrical resistivity of the samples $Ce_{1.2}Rh_2Sn_{3.8}$ and $La_{1.1}Rh_2Sn_{3.9}$ indicate that additional RE atoms replacing some Sn atoms introduces a substantial amount of disorder in the compounds. In the case of $Ce_{1.2}Rh_2Sn_{3.8}$ it leads also to the distinct lowering of the magnetic ordering temperature and a reduction of the ferromagnetic component in the magnetically ordered state. The XAS and XPS spectra recorded at high temperatures indicate that all the Ce ions in $Ce_{1.2}Rh_2Sn_{3.8}$ are in a trivalent state.

## 5. Conclusion

We presented a combined study of the electronic band structure and thermodynamic properties of $CeRh_2Sn_4$ and the reference compound $LaRh_2Sn_4$. The crystal structure of $CeRh_2Sn_4$ has been determined from single-crystal diffraction experiments.

The experimental atomic coordinates of $CeRh_2Sn_4$ are in good agreement with those obtained from electronic structure calculations within the LDA approximation and are very similar to those estimated for $LaRh_2Sn_4$. The computational crystal structure optimization as well as the analysis of charge density maps excluded a significant contribution of Ce 4f states to the chemical bonding in $CeRh_2Sn_4$. This is consistent with the Ce $L_{III}$ XAS and Ce core-level XPS spectra and the magnetic susceptibility data, which unanimously point to the stable trivalent state of Ce ions in $CeRh_2Sn_4$. Based on the magnetic part of the specific heat, a crystal field level scheme for the $Ce^{3+}$ ions has been proposed.

Thermodynamic measurements for $CeRh_2Sn_4$ reveal a magnetic ordering at $T_N \approx 3.2$ K to a noncollinear antiferromagnetic-type structure. First-principles band structure calculations confirm a magnetic ground state for $CeRh_2Sn_4$ and show significant magnetic moments only at the Ce sites. The reliability of the theoretical results has been confirmed by the comparison with the XPS valence band spectra. The electronic structure of $CeRh_2Sn_4$ is very similar to that of the reference compound $LaRh_2Sn_4$. There are indications for spin fluctuations in the dynamic magnetic susceptibility and the specific heat for both $CeRh_2Sn_4$ and $LaRh_2Sn_4$. A Fermi surface analysis shows that there are some parallel sections of the sheets which could generate nesting instabilities and be responsible for the spin fluctuation effects.

Finally, both $CeRh_2Sn_4$ and $LaRh_2Sn_4$ were found to exhibit small homogeneity ranges as described by the formula $RE_{1+x}Rh_2Sn_{4-x}$, where $0 \leqslant x \lesssim 0.2$ for Ce and $0 \leqslant x \lesssim 0.1$ in the case of La. Implantation of additional RE atoms into the $RERh_2Sn_4$ structure introduces a substantial amount of disorder. In the case of $Ce_{1.2}Rh_2Sn_{3.8}$ this leads also to a distinct lowering of $T_N$ and the weakening of the ferromagnetic component of the magnetic state. For the La-based systems the alloying reduces the strong diamagnetism.

## Acknowledgments

## References

[1] Stewart G R 2001 *Rev. Mod. Phys.* **73** 797
     Loewenhaupt M and Fischer K H 1993 *Handbook on the Physics and Chemistry of Rare Earths* vol 16, ed K A Gschneidner Jr and L Eyring (Amsterdam: North-Holland) chapter 105 p 1
     Grewe N and Steglich F 1991 *Handbook on the Physics and Chemistry of Rare Earths* vol 14, ed K A Gschneider Jr and L Eyring (Amsterdam: North-Holland) chapter 97, p 343
     Steglich F and Suellow S 2001 *Encyclopedia of Materials: Science and Technology* (Amsterdam: Elsevier) p 3746

[2] Patil N G and Ramarkrishnan S 1997 *Phys. Rev.* B **56** 3360
[3] Niepmann D, Pöttgen R, Künnen B, Kotzyba G,
    Rosenhahn C and Mosel B D 1999 *Chem. Mater.* **11** 1597
[4] Patil N G and Ramakrishnan S 1999 *Phys. Rev.* B **59** 12054
[5] Ślebarski A, Maple M B, Freeman E J, Sirvent C,
    Radłowska M, Jezierski A, Granado E, Huang Q and
    Lynn J W 2002 *Phil. Mag.* B **82** 943
[6] Kim M S, Echizen Y, Umeo K, Kobayashi S, Sera M,
    Salamakha P S, Sologub O L, Takabatake T, Chen X,
    Tayama T, Sakakibara T, Jung M H and Maple M B 2003
    *Phys. Rev.* B **68** 054416
[7] Tou H, Kim M S, Takabatake T and Sera M 2004 *Phys. Rev.* B
    **70** 100407(R)
[8] Shimada K, Namatame H, Taniguchi M, Higashiguchi M,
    Fujimori S-I, Saitoh Y, Fujimori A, Kim M S, Hirata D and
    Takabatake T 2006 *Physica* B **378–380** 791
[9] Łątka K, Kmieć R, Pacyna A W and Pöttgen R 2008 *J. Magn.
    Magn. Mater.* **320** L18
[10] Ślebarski A, Frederick N A and Maple M B 2002 *Phil. Mag.* B
    **82** 1275
    Ślebarski A, Spałek J, Gamża M and Hackemer A 2006 *Phys.
    Rev.* B **73** 205115
[11] Gamża M, Ślebarski A and Rosner H 2008 *J. Phys.: Condens.
    Matter* **20** 025201
[12] Gamża M, Schnelle W, Ślebarski A and Rosner H 2007 *Mater.
    Sci. Poland* **25** 269–74
[13] Méot-Mayer M, Venturini G, Malaman B and Roques B 1985
    *Mater. Res. Bull.* **20** 913
[14] Akselrud L G, Zavalij P Yu, Grin Yu N, Pecharsky V K,
    Baumgartner B and Wölfel E 1993 *Mater. Sci. Forum*
    **333–335** 133
[15] Baer Y, Bush G and Cohn P 1975 *Rev. Sci. Instrum.* **46** 466
[16] Koepernik K and Eschrig H 1999 *Phys. Rev.* B **59** 1743
[17] Perdew J P and Wang Y 1992 *Phys. Rev.* B **45** 13244
[18] Eschrig H 1989 *Optimized LCAO Method and the Electronic
    Structure of Extended Systems* (Berlin: Springer)
[19] Eschrig H, Koepernik K and Chaplygin I 2003 *J. Solid State
    Chem.* **176** 482
[20] Yeh J J and Lindau I 1985 *At. Data Nucl. Data Tables* **32** 1
[21] Singh D 1994 *Plane Waves, Pseudopotentials and the LAPW
    Method* (Boston: Kluwer Academic)
[22] Blaha P, Schwarz K, Madsen G, Kvasnicka D and Luitz J 2001
    *Program for Calculating Crystal Properties Wien2k* Vienna
    University of Technology (ISBN 3-9501031-1-2)
[23] Jepsen O, Burkhardt A and Andersen O K 1999 *The Program
    TB-LMTO-ASA Version 4.7* Max-Planck-Institut für
    Festkörperforschung, Stuttgart
[24] von Barth U and Hedin L 1972 *J. Phys. C: Solid State Phys.*
    **5** 1629
[25] Andersen O K 1975 *Phys. Rev.* B **12** 3060
[26] Kohout M 2004 *Int. J. Quantum Chem.* **97** 651
[27] Kohout M, Wagner F R and Grin Yu 2006 *Int. J. Quantum
    Chem.* **106** 1499
[28] Kohout M 2007 *Faraday Discuss.* **135** 43
[29] Kohout M 2008 Basin, *Version 4.3*
[30] Bader R F W 1999 *Atoms in Molecules: a Quantum Theory*
    (Oxford: Oxford University Press)
[31] Donohue J 1974 *The Structures of the Elements* (New York:
    Wiley)
[32] Emsley J 1998 *The Elements* (Oxford: Oxford University Press)

[33] Méot-Mayer M, Venturini G, Malaman B, Steinmetz J and
    Roques B 1984 *Mater. Res. Bull.* **19** 1181
[34] Skolozdra R V 1997 *Handbook on the Physics and Chemistry
    of Rare Earth* vol 24, ed K A Gschneider Jr and
    L Eyring (Amsterdam: North-Holland) chapter 167, p 400
[35] Fuggle J C, Gunnarsson O, Sawatzky G A and
    Schönhammer K 1988 *Phys. Rev.* B **37** 1103
[36] Allen J W 1985 *J. Magn. Magn. Mater.* **47/48** 168
[37] Schneider W-D, Delley B, Wuilloud E, Imer J-M and
    Baer Y 1985 *Phys. Rev.* B **32** 6819
[38] Baer Y, Hauger R, Zürcher Ch, Campagna M and
    Wertheim G K 1978 *Phys. Rev.* B **18** 4433
[39] Gamża M, Schnelle W, Ślebarski A, Burkhardt U,
    Gumeniuk R and Rosner H 2008 *J. Phys.: Condens. Matter*
    **20** 395208
[40] Gunnarsson O and Schönhammer K 1983 *Phys. Rev.* B
    **28** 4315
    Gunnarsson O and Schönhammer K 1983 *Phys. Rev. Lett.*
    **50** 604
[41] Fuggle J C, Hillebrecht F U, Zolnierek Z, Lässer R,
    Freiburg Ch, Gunnarsson O and Schönhammer K 1973 *Phys.
    Rev.* B **27** 7330
[42] Ślebarski A, Zawada T, Spałek J and Jezierski A 2004 *Phys.
    Rev.* B **70** 235112
    Gamża M, Ślebarski A and Rosner H 2008 *Eur. Phys. J.* B **63** 1
[43] Tari A 2003 *The Specific Heat of Matter at Low Temperatures*
    (London: Imperial College Press)
[44] Villars P and Calvert L D 1991 *Pearson's Handbook of
    Crystallographic Data for Intermetallic Phases* 2nd edn
    (Materials Park, OH: ASM International)
[45] De Jongh L J and Miedema A R 2001 *Adv. Phys.* **50** 947
    reprinted from De Jongh L J and Miedema A R 1974 *Adv.
    Phys.* **23** 1
[46] Selwood P W 1956 *Magnetochemistry* (New York:
    Interscience)
[47] Mott N F 1935 *Proc. R. Soc.* A **153** 699
    Calandra M and Gunnarsson O 2002 *Phys. Rev.* B **66** 205105
[48] Cornut B and Coqblin B 1972 *Phys. Rev.* B **5** 4541
[49] Yu R, Singh D and Krakauer H 1991 *Phys. Rev.* B **43** 6411
[50] Allen J W, Oh S-J, Gunnarsson O, Schönhammer K,
    Maple M B, Torikachvili M S and Lindau I 1986 *Adv. Phys.*
    **35** 275
    Lang J K, Baer Y and Cox P A 1981 *J. Phys. F: Met. Phys.*
    **11** 121
    Boring A M, Albers R C, Eriksson O and Koelling D D 1992
    *Phys. Rev. Lett.* **68** 2652
    Herbst J F, Watson R E and Wilkins J W 1978 *Phys. Rev.* B
    **17** 3089
    Herbst J F and Wilkins J W 1979 *Phys. Rev. Lett.* **43** 1760
    Anisimov V I and Gunnarsson O 1991 *Phys. Rev.* B
    **43** 7570 and references there in
[51] Wagner F R, Bezugly V, Kohout M and Grin Yu 2007
    *Chem.—Eur. J.* **13** 5724
[52] Kohout M, Wagner F R and Grin Yu 2002 *Theor. Chem. Acc.*
    **108** 150
[53] Tougaard S and Sigmund P 1982 *Phys. Rev.* B **25** 4452
[54] Gamża M, Ślebarski A and Deniszczyk J 2008 *J. Phys.:
    Condens. Matter* **20** 115202
[55] Vavassori P, Duó L and Richter M 1999 *Physica* B
    **259–261** 1120